NDT&E International 133 (2023) 102749

Contents lists available at ScienceDirect

NDT and E International

journal homepage: www.elsevier.com/locate/ndteint

Dipole modelling of temperature-dependent magnetic flux leakage

Yujue Wang [a], Yevgen Melikhov [a,b,*], Turgut Meydan [a,1]

[a] Wolfson Centre for Magnetics, School of Engineering, Cardiff University, CF24 3AA, UK
[b] Institute of Fundamental Technological Research PAS, Pawinskiego 5B, 02-106, Warsaw, Poland

ARTICLE INFO

Keywords:
Magnetic dipole model
Magnetic flux leakage
Temperature
J-A model
Thermal stress
Magnetomechanics

ABSTRACT

Due to the nonlinear coupling, assessing the direct effect of temperature on magnetic flux leakage (MFL) signal is a complicated task. If temperature induces inner stress, it makes the problem doubly difficult, so few models are available for predicting the MFL signal under this condition. To model the effect of temperature on MFL signal, the temperature-dependent magnetic dipole models are proposed. In the first case, where the direct thermal effect is involved only, the dipole model is improved via the modified temperature-dependent Jiles-Atherton (J-A) model. While in the second case, where the combined effects of temperature and thermal stress are considered, the magnetomechanical J-A parameters are further introduced into the dipole model. The thermal stress distribution around a cylindrical through-hole defect is solved by thermoelastic and solid mechanics theories. The magnetomechanical theory is employed to analyse the stress-dependent magnetisation distribution, the key parameter in the magnetic dipole model. The verified experiments are conducted on an M250-50A non-oriented grain (NO) silicon steel specimen with a cylindrical through-hole defect. And the MFL signals predicted by both proposed models agree with the experimental results. When the direct effect of temperature is involved only, the peak-to-peak amplitude of the MFL signal (MFL_{pp}) presents approximately linear dependence on temperature in the range from $-40\,^{\circ}C$ to $60\,^{\circ}C$. In addition, when both temperature and thermal stress are considered, the MFL_{pp} changes as a parabolic function of temperature, this being much more significant than the direct effect. The proposed models can act as effective tools to understand the temperature and thermal stress influences on MFL signals. They are also appropriate to solve the inverse problem of sizing the defects accurately when the temperature is involved.

1. Introduction

Magnetic flux leakage (MFL) method is widely used for the nondestructive evaluation (NDE) of defects in ferromagnetic materials. In MFL applications, specimens are magnetised, and the leaked flux due to the sudden change of permeability near geometric discontinuities is detected by MFL sensors [1,2]. The detected MFL signals are then used inversely to estimate the sizes of defects. In addition to using peak-to-peak amplitude and full width at half maximum (FWHM) to solve the inverse problem [3,4], there are a few studies that have paid attention to the effects of stress [5–7] and scanning speed [8,9] on MFL. However, to the best of our knowledge, few attempts have been made to analyse the thermal effect on MFL signals.

It is hard to maintain a constant temperature in most machines and structures. Friction, Joule loss and eddy current could easily heat the devices. And there are many structures installed outdoors and experiencing variations in temperatures on a daily basis, for example, railway and pipeline. The maximum value of magnetisation of the hysteresis loop has been experimentally observed to decrease more than 25% with the temperature variation of 100 K [10–13]. According to magnetic dipole models [6,14], magnetisation, which is related to the surface magnetic charge density, could significantly influence MFL signal. Therefore, the change of temperature should have a noticeable influence on MFL signal.

Besides, the temperature rarely independently influences MFL signal. The environmental temperature may lead to thermal stress where, for example, the stress value in a seamless track of a high-speed railway could reach tens or even hundreds of MPa [15,16]. The thermal stress may also have a noticeable indirect influence on the MFL detection results. Wang et al. [6] found that 100 MPa tensile stress caused an increase of 24% in the peak-to-peak amplitude of the MFL signal (MFL_{pp}) for the cylindrical hole defect in the plate. Besides, a decrease of 11% in

* Corresponding author. Wolfson Centre for Magnetics, School of Engineering, Cardiff University, CF24 3AA, UK.
E-mail address: Melikhov@cardiff.ac.uk (Y. Melikhov).
[1] Deceased.

https://doi.org/10.1016/j.ndteint.2022.102749
Received 28 March 2022; Received in revised form 11 September 2022; Accepted 21 September 2022
Available online 25 September 2022

MFL_{pp} caused by 100 MPa tensile stress for the circumferential square-notch defect on the surface of rod sample was observed [7]. In addition, Mandal et al. [5] experimentally investigated the stress-dependent MFL signals in in-service oil and gas pipelines, whose amplitudes changed more than 40% caused by the line pressure stress. Therefore, quantitative evaluation of the direct and indirect thermal effects on MFL is vital to accurately size the defect in the inverse problem.

This paper aims to propose improved magnetic dipole models that consider the direct effect of temperature and the combined effects of temperature and thermal stress for quantitative evaluation of both thermal effects on MFL. The modelling object is a thin sheet specimen with a cylindrical through-hole. This paper is organised as follows. In Section 2, the temperature-dependent dipole models are proposed based on the magnetothermal and magnetomechanical Jiles-Atherton (J-A) hysteresis models. In Section 3, the details about the verification experiments, including the specimen tempered procedure and the configuration of the MFL sensor, are explained. Both the performance and limitations of the proposed model are discussed in Section 4. Finally, the major findings of this study are discussed in Section 5.

2. Temperature-dependent magnetic dipole models

2.1. The dependency of MFL on temperature only

In this paper, the magnetic dipole model is extended based on our previous improved temperature-dependent J-A models [17] using a reference temperature instead of absolute zero and developing an equation for the temperature dependence of reversibility factor, c, whose item for initial susceptibility was previously assumed to be a constant. The thermal effect can be incorporated into the J-A model by expressing the five key hysteresis parameters.

The temperature-dependent parameters saturation magnetisation, M_{st}, the domain wall pinning factor, k, the domain density, a, the domain coupling, α, and the reversibility factor, c, are given by [17].

$$M_{st}(T) = M_{st}(T_r)\left(\frac{T_c - T}{T_c - T_r}\right)^{\beta_1} \tag{1}$$

$$k(T) = k(T_r)e^{\left(\frac{T_r - T}{\beta_2 T_c}\right)} \tag{2}$$

$$a(T) = a(T_r)e^{\left(\frac{T_r - T}{\beta_3 T_c}\right)} \tag{3}$$

$$\alpha(T) = \alpha(T_r)e^{\left(\frac{T_r - T}{\beta_3 T_c}\right)}\left(\frac{T_c - T_r}{T_c - T}\right)^{\beta_1} \tag{4}$$

$$c(T) = c(T_r)e^{\left(\frac{T_r - T}{\beta_4 \beta_3 T_c}\right)}\left(\frac{T_c - T_r}{T_c - T}\right)^{\beta_1} \tag{5}$$

where T_r is the reference temperature (for example, 20 °C), T_c is the Curie temperature, and β_1, β_2, β_3, β_4 are the material-dependent critical exponents.

Therefore, the M-H hysteresis model can be modified as [17].

$$\frac{dM(T)}{dH} = \frac{\chi_M(T)}{k(T) - \alpha(T)\chi_M(T)} \tag{6}$$

where

$$\chi_M(T) = \delta_m[M_{an}(T) - M(T)] + k(T)\delta c(T)\frac{dM_{an}(T)}{dH_e(T)} \tag{7}$$

where

$$\delta_m = \begin{cases} 0 : \dfrac{dH}{dt} < 0 \text{ and } M_{an}(H_e) - M(H) > 0 \\ 0 : \dfrac{dH}{dt} > 0 \text{ and } M_{an}(H_e) - M(H) < 0 \\ 1 : otherwise \end{cases} \tag{8}$$

Let us now investigate the direct effect of temperature on MFL, for which a new dipole model is introduced on the base of the previous models for a cylindrical through-hole defect on a sheet [6,14]. The cylindrical through-hole defect is located in the sample's centre. The radius (R) of the defect is much smaller than the width (W) of the sheet but larger than its thickness (b). As shown in Fig. 1, the external applied magnetic field ($\mathbf{H}$) is aligned in the positive direction of the y-axis. The top surfaces of sheet and defect are in xy-plane, and the defect is symmetric about xz-plane. The surface of defect along the negative y-axis is assigned with positive magnetic charge density (or north polarity), while the other half of the cylindrical surface is assigned with negative magnetic charge density (or south polarity).

Infinitesimal element with an area of dS along the defect surface orients at an angle of θ relative to the positive direction of x-axis. The element of dS carries a magnetic charge of dρ, which generates a magnetic field of d$\mathbf{H}_T$ at a point $P(x, y, h)$ in the space. The formula to calculate the magnetic field of d$\mathbf{H}_T$ is

$$d\mathbf{H}_T = \frac{1}{4\pi}\frac{\mathbf{r}}{r^3}d\rho \tag{9}$$

where $\mathbf{r}$ is a vector pointing from the element of dS to $P(x, y, h)$, and r is the distance between the dS and point P.

The magnetic charge density, ρ, on the surface element dS is given by

$$d\rho = \mathbf{M_T}\cdot\mathbf{n}dS = M_T\ sin\ \theta dS \tag{10}$$

where

$$M_T = \left\{\frac{\mu_{r_T} - 1}{\mu_{r_T} - N_y[\mu_{r_T} - 1]}\right\}H_{e_T} \tag{11}$$

where

$$\mu_{r_T} = \frac{1}{\mu_0}\left(\frac{M(T)}{H_0} + 1\right) \tag{12}$$

H_{e_T} is the effective magnetic field at a certain temperature, and N_y denotes the demagnetising factor corresponding to the y-axis is given by [18]

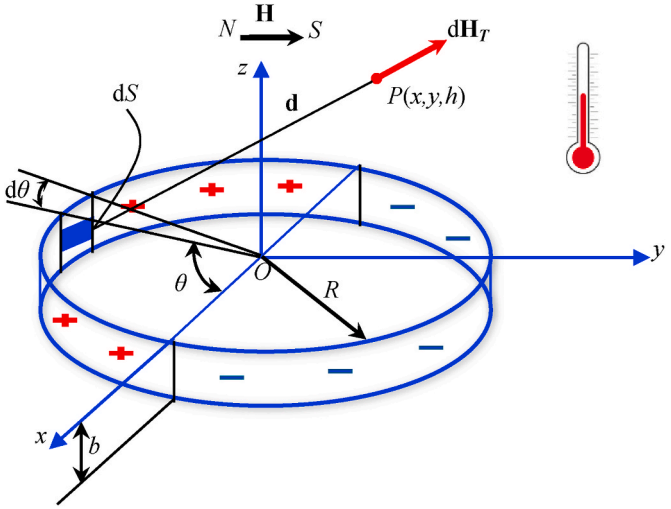

Fig. 1. Dipolar representation of a cylindrical through-hole defect.

$$N_y = \frac{\eta\pi^2 - 4}{4\pi\eta^2} \tag{13}$$

where $\eta = R/b \gg 1$. The demagnetising factor depends on the applied magnetic field and defect shape and size.

Substituting Eq. (10) ~ (13) into Eq. (9), the magnetic field generated by the magnetic charge can be computed by the expression:

$$d\mathbf{H}_T = \frac{1}{4\pi}\frac{\mathbf{r}}{r^3}\left\{\frac{\mu_{r_T} - 1}{\mu_{r_T} - N_y\left[\mu_{r_T} - 1\right]}\right\} H_{e_T} R sin\theta d\theta dz \tag{14}$$

The components of $d\mathbf{H}_T$ in the Cartesian coordinate system are given by

$$dH_{Tx} = \frac{M_T}{4\pi}\frac{r_x}{r^3} R sin\theta d\theta dz \tag{15}$$

$$dH_{Ty} = \frac{M_T}{4\pi}\frac{r_y}{r^3} R sin\theta d\theta dz \tag{16}$$

$$dH_{Tz} = \frac{M_T}{4\pi}\frac{r_z}{r^3} R sin\theta d\theta dz \tag{17}$$

The integration in Eq. (14) ~ (17), along with Eq. (6), can be performed using, e.g., the Runge-Kutta method. The improved magnetic dipole model, together with Eq. (1) ~ (8) that relate change of temperature and magnetisation variation, provides a pathway to investigate the effect of temperature on the MFL signals.

2.2. The combined effects of temperature and thermal stress on MFL

The model presented above can be used to model the direct effect of temperature itself on MFL signal. However, the temperature gradient and variation in a sample may induce inner stresses, which could indirectly affect MFL signals. Generally, there are two types of inner stresses induced by temperature: Type 1 is caused by asymmetric temperature distribution in a structural component. For example, a long or sizeable structural component is exposed to gradient environmental temperatures such as railway

$$\varepsilon_{T1} = \alpha_T(T_1 - T_2) \tag{18}$$

And type 2 is resulted from two materials with different coefficients of thermal expansion (CTE) fixed together, such as multilayer plate:

$$\varepsilon_{T2} = (\alpha_{T1} - \alpha_{T2})(T_r - T) \tag{19}$$

where ε_{T1} and ε_{T2} are the thermal strains induced via types 1 and 2, respectively, and α_{T1} and α_{T2} are the larger and the smaller CTEs of two materials, respectively, and T_r is the reference temperature [19].

The experimental conditions related to this work can be described via the second type, where two components with different CTE are fixed together, as shown in Fig. 2.

The thermal stress, σ, could be inferred from the thermal strain below elastic limitation [20].

$$\begin{bmatrix}\sigma_{xx}\\ \sigma_{yy}\\ \sigma_{zz}\\ \sigma_{xy}\\ \sigma_{xz}\\ \sigma_{yz}\end{bmatrix} = \frac{E}{(1+\nu)(1-2\nu)}\begin{bmatrix}1-\nu & \nu & \nu & 0 & 0 & 0\\ \nu & 1-\nu & \nu & 0 & 0 & 0\\ \nu & \nu & 1-\nu & 0 & 0 & 0\\ 0 & 0 & 0 & \frac{1-2\nu}{2} & 0 & 0\\ 0 & 0 & 0 & 0 & \frac{1-2\nu}{2} & 0\\ 0 & 0 & 0 & 0 & 0 & \frac{1-2\nu}{2}\end{bmatrix}\begin{bmatrix}\varepsilon_{xx}\\ \varepsilon_{yy}\\ \varepsilon_{zz}\\ \varepsilon_{xy}\\ \varepsilon_{xz}\\ \varepsilon_{yz}\end{bmatrix} \tag{20}$$

where σ_{xx} and ε_{xx} are the x-axis component of thermal stress and strain, E is Young's modulus and ν is Poisson's ratio. Assuming there is no fixed constraint along the z-axis, for an isotropic lamination specimen, σ_{zz}, σ_{xz}, σ_{yz} are approximately equal zero, $\sigma_{xy} = \tau_{xy}$ and $\varepsilon_{xy} = \gamma_{xx}/2$, hence, Eq. (20) can be simplified as

$$\begin{bmatrix}\sigma_{xx}\\ \sigma_{yy}\\ \tau_{xy}\end{bmatrix} = \frac{E}{(1+\nu)(1-2\nu)}\begin{bmatrix}1-\nu & \nu & 0\\ \nu & 1-\nu & 0\\ 0 & 0 & \frac{1-2\nu}{2}\end{bmatrix}\begin{bmatrix}\varepsilon_{xx}\\ \varepsilon_{yy}\\ \gamma_{xy}\end{bmatrix} \tag{21}$$

The multilayer structure shown in Fig. 2 could induce thermal stress when the temperature changes due to the considerable difference CTEs between two materials (e.g., ceramic glass 1×10^{-7} $1/^{\circ}C$ and non-oriented grain silicon steel 11.9×10^{-6} $1/^{\circ}C$). As there is no constraint along the x-axis, the sample can be considered expanding freely along the x-axis. Hence, the thermally induced strain along the x-axis is approaching zero. Therefore, Eq. (21) can be expressed by

$$\begin{bmatrix}\sigma_{xx}\\ \sigma_{yy}\\ \tau_{xy}\end{bmatrix} = \frac{E}{(1+\nu)(1-2\nu)}\begin{bmatrix}1-\nu & \nu & 0\\ \nu & 1-\nu & 0\\ 0 & 0 & \frac{1-2\nu}{2}\end{bmatrix}\begin{bmatrix}0\\ \varepsilon_{yy}\\ \gamma_{xy}\end{bmatrix} \tag{22}$$

In this structure, the thermally induced inner stress of the steel sample alone y-axis, which is parallel to the magnetic field, H, is employed in the following calculation. According to the analytical expressions reported by Timoshenko, the stress along the surface of the cylindrical through-hole defect can be expressed as [6,20].

$$\sigma_\theta = \sigma_{yy}(1 + 2\,cos\,2\theta) \tag{23}$$

According to magnetomechanical theories, the effective field can be given by [6,21,22].

$$H_e = H + \alpha M + \frac{3\sigma}{2\mu_0}\frac{d\lambda}{dM} = H + \tilde{\alpha}M \tag{24}$$

where magnetostriction $\lambda(\sigma, M) \approx \gamma_0 + (\gamma_{11} + \gamma_{12}\sigma)M^2$. Hence, the temperature-dependent M-H hysteresis model (6) can be modified as

$$\frac{dM(T)}{dH} = \frac{\chi_M(T)}{k(T)\delta - \tilde{\alpha}(T)\chi_M(T)} \tag{25}$$

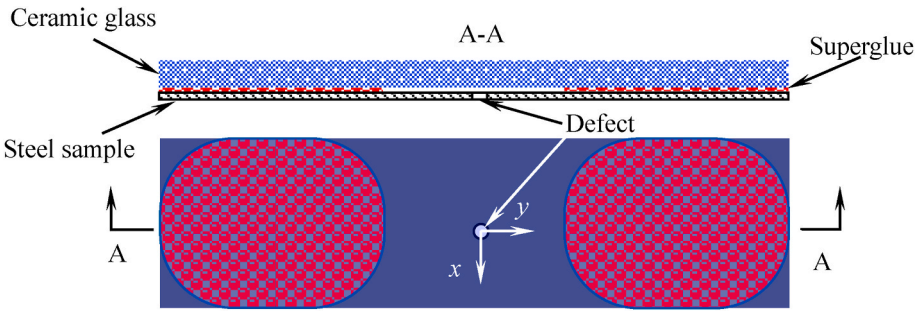

Fig. 2. The thermally induced stress structure.

Considering both direct and indirect effects of temperature, the magnetisation, which is related to the surface magnetic charge density (ρ), along the defect wall can be expressed as

$$M_{T\sigma}(\theta)=\left\{\frac{\mu_{r_{T\sigma}}(\theta)-1}{\mu_{r_{T\sigma}}(\theta)-N_y\left[\mu_{r_{T\sigma}}(\theta)-1\right]}\right\}H_{e_{T\sigma}}(\theta) \tag{26}$$

where

$$\mu_{r_{T\sigma}}(\theta)=\frac{1}{\mu_0}\left(\frac{M(T,\sigma,\theta)}{H}+1\right) \tag{27}$$

and

$$H_{e_{T\sigma}}(\theta)=H+\widetilde{\alpha}_T(\theta)M(T,\sigma,\theta) \tag{28}$$

Hence, the spatial magnetic field generated by the magnetic charge can be modified as

$$d\mathbf{H}_{T\sigma}(\theta)=\frac{1}{4\pi}\frac{\mathbf{r}}{r^3}\left\{\frac{\mu_{r_{T\sigma}}(\theta)-1}{\mu_{r_{T\sigma}}(\theta)-N_y\left[\mu_{r_{T\sigma}}(\theta)-1\right]}\right\}H_{e_{T\sigma}}(\theta)Rsin\theta d\theta dz \tag{29}$$

The components of $d\mathbf{H}_{T\sigma}$ in the Cartesian coordinate system are given by

$$dH_{T\sigma x}=\frac{M_{T\sigma}(\theta)}{4\pi}\frac{r_x}{r^3}Rsin\theta d\theta dz \tag{30}$$

$$dH_{T\sigma y}=\frac{M_{T\sigma}(\theta)}{4\pi}\frac{r_y}{r^3}Rsin\theta d\theta dz \tag{31}$$

$$dH_{T\sigma z}=\frac{M_{T\sigma}(\theta)}{4\pi}\frac{r_z}{r^3}Rsin\theta d\theta dz \tag{32}$$

Eq. (30)~(32), along with Eqs. (6) and (25) can compute the magnetic field using the Runge-Kutta integration method. The improved magnetic dipole models provide a tool for understanding the effects of temperature and thermal stress on the MFL signal. It should be noticed that Eq. (13) gives the approximation of demagnetising factor rather than the exact value. Besides, the effect of magnetic compression [1,23] is not taken into account in this paper. These may cause errors in calculating the absolute value of magnetic flux leakage. In the subsequent analysis, the MFL signals for different temperature cases are normalised by the case at 20 $^\circ C$ (reference temperature) so that the magnitude of surface charge density does not appear in the computation [6,14]. Although the modified model is used in the case of a sample having a regular shape with a simple defect, the applicability of the proposed model is not limited to this case only, and samples with other shapes might also be treated. For example, the stress distributions for elliptical holes and ellipsoidal inclusion in plate can be derived from the classical elastic mechanics [20]. Besides, demagnetising factors of various ellipsoids have been mathematically calculated and verified [18]. Moreover, Trevino et al. [24] have improved the dipole model to simulate ellipsoidal defect shape and even more complicated defect shapes. These mathematical models provide the potential to analyse magnetic flux leakage caused by defects with various shapes. Also note that the cylindrical hole used in this research is a particular case of elliptical hole defects.

3. Experiments

3.1. The MFL experiments considering the exclusively thermal effect

The MFL experiments that investigate the direct effect of temperature itself on MFL are conducted on an M250-50A non-oriented (NO) grain silicon steel with 0.45 mm in thickness, 30 mm in width and 190 mm in length. Such a shape of the sample could be fast and evenly heated/cooled. A cylindrical through-hole defect is machined at the geometric centre of the specimen with a radius of 2 mm. One U-shape yoke wound by exciting coil together with the other yoke are used to provide a steady static magnetic field along the tensile direction for specimen magnetisation (as seen in Fig. 3). The coil is fed by 2 A direct current. According to the measurement of Gaussmeter, it could provide a 1500 A/m magnetic field around the centre of the sample.

A Hall effect sensor (ACS70310LKTATN-010B5–C manufactured by ALLEGRO), which has ultralow thermal drift, high sensitivity and wide measurement range, is used to measure the MFL signal. A motorised XYZ linear translation stage from Thorlabs with a minimum achievable incremental movement of 0.1 μm is used to move the sensor along the sample surface in precise steps. The measurement setup is mounted on a non-magnetic breadboard, which is located in the environmental chamber (HC4033 from Vötsch). Measurements are made by scanning the sensor across the centre of the through-hole defect, with a fixed scan step size and sensitive element lift-off of 0.1 mm and 1.5 mm, respectively.

In MFL experiments, the sample and measurement setup are cooled down from 20 $^\circ C$ to −40 $^\circ C$ with 10 $^\circ C$ decrements in temperature and then heated up to 60 $^\circ C$ with 10 $^\circ C$ increments. The temperatures are set step by step. At each set temperature point, the measurement will not be implemented until the temperature is steady for more than 10 min, which would allow even cooling or heating of the sample and avoid the effect of temperature variation. The magnetic field measurements are repeated 100 times at each motion step, and the mean values are obtained. The entire process is repeated five times to reduce the measurement error.

Before the MFL experiments, the specimens are annealed at 400 $^\circ C$ for 2 h to relieve the residual stress. Then, the hysteresis curves of the specimen without defect are measured at different temperatures by the quasi-static hysteresis measurement system to determine the key parameters of the temperature-dependent J-A model as discussed in Ref. [17]. The hybrid GA-PSO algorithm (GA and PSO stand for Genetic Algorithm and Particle Swarm Optimisation respectively) is used to identify those parameters, which are listed in Table 1.

3.2. The MFL experiments considering the combined effects of temperature and thermal stress

In MFL experiments that study the combined effects of temperature and thermal stress on MFL, the NO steel is glued to the ceramic glass (Schott Zerodur), whose CTE ($1\times10^{-7}\ ^\circ C^{-1}$) is much smaller than NO steel ($11.9\times10^{-6}\ ^\circ C^{-1}$), at room temperature (20 $^\circ C$). The maximum thermal stress should be less than the nominal yield stress of NO steel (344 MPa) so that the minimum temperature should be higher than −20 $^\circ C$. Besides, when the temperature is higher than room temperature, the NO steel is compressed, and it could cause the sample bending, which makes the calculation complicated and uncertain. Therefore, the measurements similar to the first MFL experiments are repeated between −10 $^\circ C$ and 20 $^\circ C$.

The experiments outside the aforementioned temperature range are also conducted. Before doing the measurements in the temperature range from 30 $^\circ C$ to 60 $^\circ C$, the sample needs to be taped on the ceramic glass to reduce the change of lift-off caused by bending. Since the temperature in range −40 $^\circ C$ to −20 $^\circ C$ may induce plastic deformation, the experiments in this range are implemented at the end of the measurement list.

The experimental conditions related to this work can be described via the second type of thermal stress, where two components with different CTE are fixed together as shown in Fig. 2. The measurement processing is analogous to the aforementioned MFL experiments considering direct effect of temperature only. Though the non-magnetic ceramic glass is inserted into the yoke gap, which decreases the magnetic field to around 800 A/m, it is still high enough for the soft magnetic material NO steel.

Prior to the MFL experiments for investigation of the combined effects, the key parameters of magnetostriction are measured by the AC magnetostriction system. The measured magnetostriction curve is

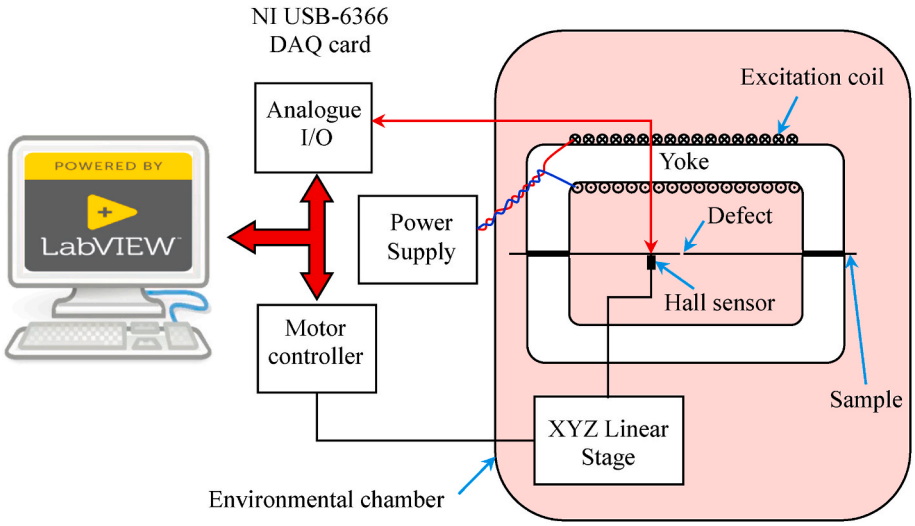

Fig. 3. The experimental setup for the measurement of MFL induced by the defect on NO silicon steel.

Table 1
The temperature-dependent parameters of J-A model for M250-35A non-oriented electrical steel.

	Parameters	value	Sources
Parameters of J-A model at 20 °C	Reversibility parameter, c	0.6799	Ref. [17]
	Pining parameter, k	103.8603 (A/m)	
	Domain density, a	65.5559 (A/m)	
	Saturation magnetisation, M_s	1.7157×10^{6} (A/m)	
	Coupling factor, α	1.2493×10^{-4}	
The coefficients of the temperature-dependent J-A model	The thermal coefficient for magnetisation, β_1	0.3981	
	The thermal coefficient for pinning constant, $\beta_2\approx\beta_3$	0.2336	
	The thermal coefficient for reversibility factor, β_4	1.7220	

Table 2
The parameters of magnetomechanical J-A model for M250-50A NO electrical steel.

	Parameters	value	Sources
Magnetostriction coefficients	γ_{11}	-2.58×10^{-19} (A^{-2} m^2)	Fitting to the measured curves
	γ_{12}	7.37×10^{-27} (A^{-2} m^2 Pa^{-1})	
Coefficient of thermal expansion	CTE of ceramic glass	1.00×10^{-7} $°C^{-1}$	Refs. [29,30]
	CTE of NO steel	11.90×10^{-6} $°C^{-1}$	
The parameters of elastic mechanics	Young's Modulus, E	205 (GPa)	Ref. [31]
	Poisson's ratio, ν	0.28	

plotted in Fig. 6, and its values are listed in Table 2. Besides, Young's Modulus (E) and Poisson's Ratio (ν) are determined and listed in Table 2.

4. Results and discussion

4.1. The direct effect of temperature on MFL

The magnetic hysteresis loops of the M250-50A NO steel strip have been measured using a computer-controlled hysteresis loop tracer at a quasi-DC field as described in Ref. [17]. The measurement system is subject to various temperatures that are controlled by the environmental chamber. The temperature-dependent parameters of J-A model are listed in Table 1.

The simulated MFL results along the y-axis at $-40\ °C$, $20\ °C$ and $60\ °C$ using the identified parameters are plotted in Fig. 4, compared with the measurements results. All the simulated MFL signals are normalised by the maximum amplitude of the MFL signal at $20\ °C$. The same operation is applied to the measured MFL signals. It can be found that both the shape and highest amplitude of the simulated MFL signals are consistent with the measured ones. It indicates that the proposed dipole model is adequate to predict the temperature dependent MFL accurately. The distances between two minimum values of the measured MFL signals are slightly narrower than the simulated. It may be caused by the effect of magnetic compression [1,23], which is not considered in the analytical model. But this will have little influence on sizing the defect as the simulated full width at half maximum (FWHM) are close to the experimental ones.

To evaluate the relationship between the MFL signal and the temperature quantitatively, the peak-to-peak amplitudes (MFL_{pp}) of the normalised MFL signals are estimated and plotted in Fig. 5. It can be

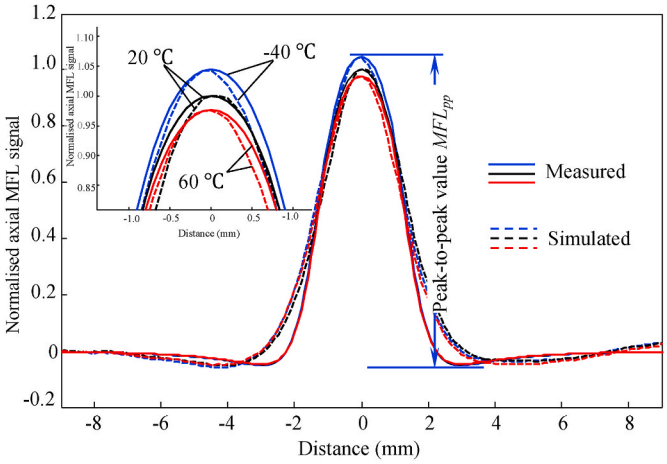

Fig. 4. The measured (solid lines) and simulated (dashed lines) axial components of MFL along the y-axis under different temperature conditions. The inset shows the enlarged view of the maximum values of normalised MFL signals.

found that the dependence of the amplitude of MFL signal on temperature obtained from the experiment agrees with the simulated ones with a coefficient of determination higher than 0.9. When the temperature range expands wider, an approximately exponential decrease will be demonstrated since the key parameters of J-A model exponentially decrease with the increase of temperature. Hence, though the increase of temperature from $-40\ ^{\circ}C$ to $60\ ^{\circ}C$ results in a decrease of the peak-to-peak amplitude of MFL signals by just 6.10%, it does not mean that the effect of temperature can be omitted when defect dimensions are estimated by the MFL method. Besides, in the case that the environmental temperatures are far from Curie temperature, it shows an approximately linear function with a goodness of fit higher than 0.9.

4.2. The combined effects of temperature and thermal stress on MFL

The magnetostriction coefficients need to be determined before calculating the MFL field influenced by temperature and thermal stress. The magnetostriction (λ) *vs* magnetisation (M) butterfly loop measured at 0 MPa is plotted in Fig. 6a. The half magnetostriction butterfly loop is more complex than measured at a low magnetic field [17,25] since the domain activities experience more complex processes.

At low magnetic field marked as region ***a***, the external field moves the domain walls leading to the increase of the volume of the domains closest to the field at the sacrifice of the other domains. In this region, the magnetostriction results from the motion of the 90°and 180° domain walls. Due to the displacement of 180° domain walls and the suppression of 90° domain walls, the sample elongates slightly with the magnetisation until 1.0×10^6 A/m. Besides, the magnetostriction may also excurse a slight decrease due to the reversible magnetisation and domain rotation. With the increase of magnetisation in region ***b***, the annihilation of the 180° walls starts, and the 90° domain walls rotate towards the magnetic field direction. These result in the rapid increase of magnetostriction with magnetisation, and finally the magnetostriction reaches its saturation in region ***c***, where the domain closest to the field occupies the whole grain. But continuing to increase the magnetic field, the rotation of the domain becomes dominant in the magnetisation of the whole specimen. Since the spontaneous elongation of the domain becomes smaller or even negative when the domain magnetisation rotates from the crystal axis [26], the magnetostriction decreases with magnetisation as shown in region ***d***. When the magnetisation drops from its maximum value, the domains rotate back to its crystal axis in region **e** and then the 90° domain walls re-emerge in region ***f***. In region ***g***, the magnetostriction sharply decreases to zero at 8.7×10^5 A/m and with the decrease of magnetisation, the magnetostriction reaches its minimum value around -0.07 μm/m. It finally returns back to zero at $M = 0$ A/m in region ***h***. It can be found that the change of magnetostriction from saturation to zero is much faster than that from zero to saturation due to the anisotropic energy of the grain. The upward and return curves of the butterfly loop follow different paths due to the irreversible magnetisation process in domains [27].

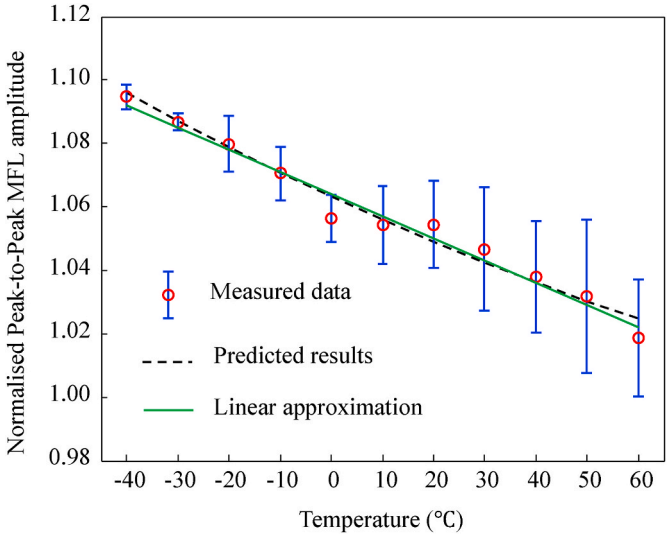

Fig. 5. The measured and predicted peak-to-peak amplitudes of the normalised MFL signals obtained from different temperatures.

To fit the complicated magnetostriction loop is not an easy task. Jiles et al. [28] proposed an infinite series to empirically model the relation between magnetostriction and magnetisation. For example, the eight-degree polynomial could approximate the average of magnetostriction as shown in Fig. 6a. However, it is impossible to model the stress-dependent MFL due to the infinite or massive parameters. The magnetostriction is generally simplified as a parabolic function of magnetisation. Since the sample is magnetised at high field, the parabolic approximation is fitted at high magnetisation in regions ***c*** to ***e*** of the λ *vs* M curves, and the coefficient γ_{11} is determined as -2.58×10^{-19} ($A^{-2}\,m^2$). The determination of the coefficient γ_{12} needs the fitting to the magnetostriction measured under stress. But the value of γ_{12} is so small that the fitting result may be altered significantly with slightly different measured loops. The terms $\gamma_{11} + \gamma_{12}\sigma$ as one coefficient could obtain a few parabolic fitting coefficients under various stresses, as shown in Fig. 6b. The slope of fitting coefficient as a linear function of stress can determine the value of γ_{12}, which is around $7.37 \times 10^{-27}(A^{-2}{\cdot}m^2{\cdot}Pa^{-1})$ according to the measurements.

Here, the MFL signal influenced by the combined effects of temperature and thermal stress can be simulated using the parameters listed in Table 2. However, only a limited temperature range is suitable for the model verification due to elastic limitation in tension and bending in compression. The MFL signals simulated and measured at $-10\ ^{\circ}C$, $0\ ^{\circ}C$, $10\ ^{\circ}C$, and $20\ ^{\circ}C$ are normalised by the maximum amplitudes of the calculated and experimental MFL signals at $20\ ^{\circ}C$, respectively. The predicted MFL results along the y-axis are plotted in Fig. 7 and are compared with the experimental ones. It can be found that both the shapes and highest amplitudes of the predicted MFL signals could coincide well with the experimental results, which manifests that the proposed dipole model is adequate to predict the combined effects of temperature and thermal stress on MFL with high accuracy.

To evaluate the relationship between the MFL signal and the temperature quantitatively, the peak-to-peak amplitudes (MFL_{pp}) of the normalised MFL signals are calculated and plotted in Fig. 8. It can be found that the dependence of MFL_{pp} on the temperature obtained from the experiment agrees with the simulated ones with a coefficient of determination higher than 0.9. The value of MFL_{pp} demonstrates the approximately linear decreasing trend with increasing temperature from $-10\ ^{\circ}C$ to $20\ ^{\circ}C$. The temperature cooling down $30\ ^{\circ}C$ from room temperature leads to an increase of 6.87% in the amplitude of the MFL signal, which is much larger than that considering direct effect only (2.04%). Hence, it needs to be considered in precise defect sizing using the MFL method.

Both the shapes and the highest amplitudes of the predicted MFL signals are consistent with the measured results, indicating that the proposed improved dipole model is adequate to predict the effect of temperature itself and the combined effects of temperature and thermal stress on MFL with high accuracy. However, several limitations of the proposed magnetic dipole model should be stated. First of all, before applying the temperature-dependent dipole model, prior knowledge of the material and defect should be acquired, including the hysteresis curve of the material measured at various temperatures, its magnetostriction loops obtained at different stress conditions and the stress distribution around the defect. Besides, the model is not adequate to precisely deal with the defects with complex shapes due to the difficulty in calculating the demagnetising factor and stress concentration. Furthermore, one of the factors that limit the applicability of the J-A magnetomechanical model using Eq. (24) ~ (32) to simulate the MFL signal is the domain coupling factor α. In this case, its value is so small

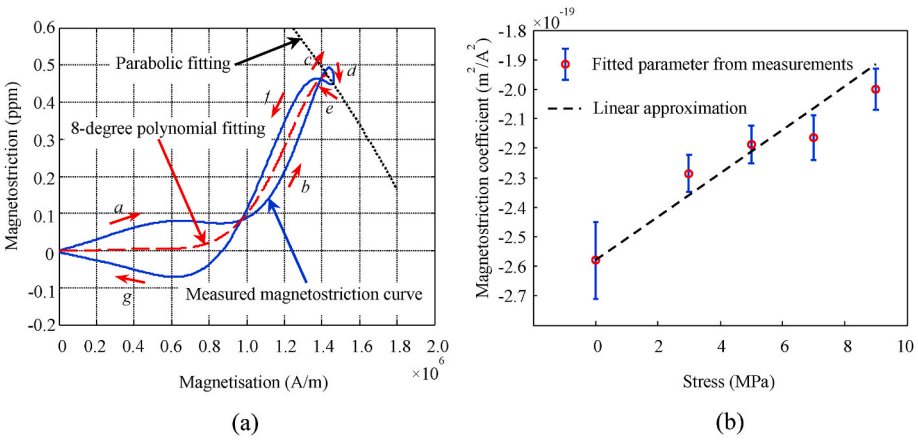

Fig. 6. (a) The measured half magnetostriction butterfly loop for M250-50A NO steel without external stress. (b) The magnetostriction coefficient of M250-50A NO steel fitted under various stresses using parabolic function.

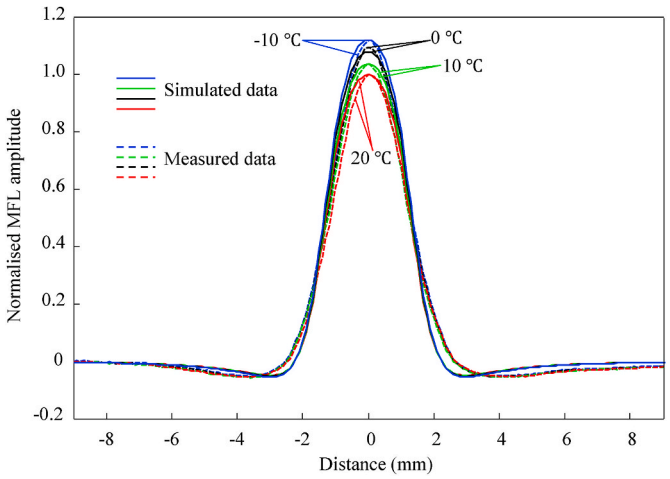

Fig. 7. The measured (dashed lines) and simulated (solid lines) axial components of MFL along the *y*-axis under different temperature conditions.

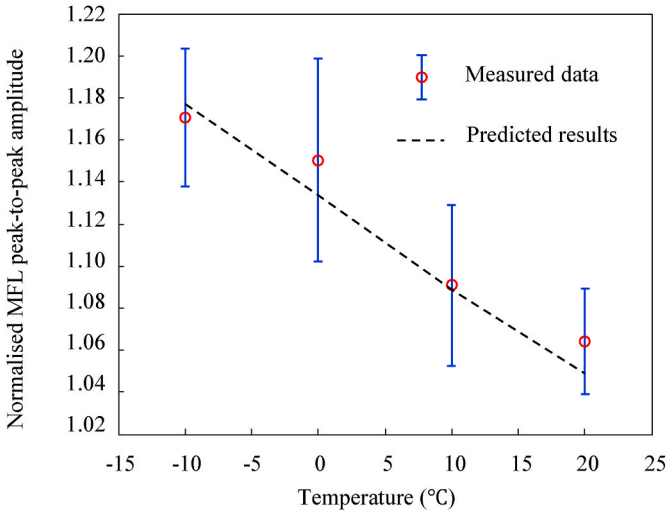

Fig. 8. The measured and predicted peak-to-peak amplitudes of the normalised MFL signals obtained from different temperatures.

that it can easily become lower than zero with thermal stress. Therefore, there are a few areas on the defect wall that cannot be calculated using the dipole model when the temperature is far from the reference temperature. These blank data are filled using cubic spline interpolation since the heterogeneous distribution of magnetisation follows periodic change with angle. In the case of outliers during interpolating, the maximum and minimum interpolation values should be limited. But it is necessary to mention that the model would work better in a magnetically harder material.

For a defect with a given shape and size, since the relative permeability satisfies $\mu_r(\theta) \gg 1$, the differential of both sides of Eq. (31) with respect to the temperature can be approximated to the differential with regard to thermal stress to simplify the evaluation of the effect of temperature on the MFL signal

$$\frac{\partial H_{T\sigma y}}{\partial T} \approx K\left(\frac{\partial \tilde{\alpha}}{\partial T}\cdot M + \frac{\partial M}{\partial T}\cdot \tilde{\alpha}\right) \approx K\left(\frac{\partial \tilde{\alpha}}{\partial \sigma_T}\cdot M + \frac{\partial M}{\partial \sigma_T}\cdot \tilde{\alpha}\right) \tag{33}$$

where K is related to the geometrical size. Eq. (33) has been proven to be an approximate four-order polynomial [6]. If omitting the high-order items, the dominant contribution should be owed to

$$\frac{\partial \tilde{\alpha}}{\partial \sigma_T} = \frac{(3\gamma_{11} + 6\gamma_{12}\cdot\sigma)}{\mu_0} \tag{34}$$

It implies that the differential of leakage field $H_{T\sigma y}$ with respect to temperature T could be approximate to that of $\tilde{\alpha}$ with regard to thermal stress σ_T, which is a linear function. Therefore, the dependency of leaked magnetic field caused by defect $H_{T\sigma y}$ on temperature T could be approximate to a parabolic function.

The experiments in the cases of the temperature exceeding the limited range of Fig. 8 are carefully conducted. The measured peak-to-peak values of MFL signals after normalisation are plotted in Fig. 9. It can be found that a parabolic approximation could fit well the measured data with fitting goodness higher than 0.9. For the ease of visual analysis, the parabolic dependency of the amplitude of the MFL amplitude on the combined effects of temperature and thermal stress is presented. Temperature cooling down from 60 °*C* to −40 °*C* leads to an increase of 35.99% in the amplitude of the MFL signals and should be considered in the inverse problem for defect sizing.

5. Conclusion

The temperature-dependent dipole models were proposed to understand and predict the direct and indirect effects of temperature on

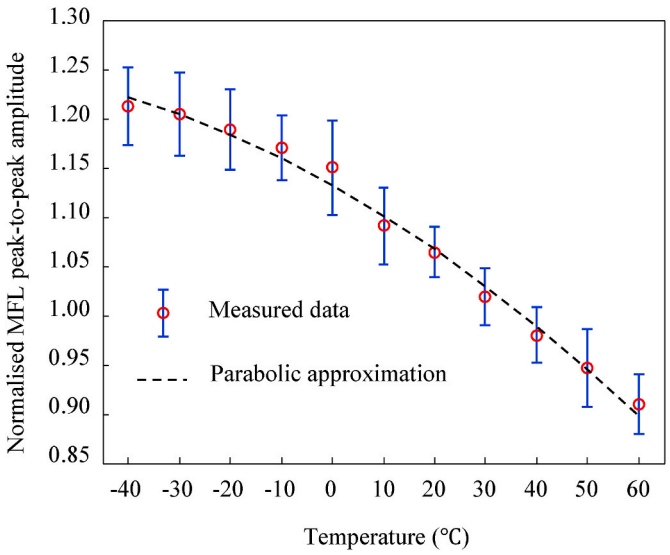

Fig. 9. The approximation of MFL peak-to-peak amplitude as a parabolic function of temperature.

MFL induced by a cylindrical through-hole in a ferromagnetic sheet analytically. The magnetic dipole model, which considered the direct effect of temperature only, was established to predict the dependency of the amplitude of the MFL signal on the temperature. Besides, the thermal stress distribution around the defect was solved using thermoelastic and solid mechanic theories. Subsequently, the temperature-dependent magnetic dipole model considering the combined effects of temperature and thermal stress was developed.

Temperature experiments were carefully arranged to measure the MFL signals induced by a cylindrical through-hole in an M250-50A NO silicon steel in the environmental chamber. In the case where the direct effect of temperature itself was involved, the temperature heating 100 $^{\circ}C$ from -40 $^{\circ}C$ resulted in a decrease of 6.10% in the peak-to-peak amplitude of the MFL signal, which fitted with the simulated ones well. Considering the combined effects of temperature and thermal stress, the magnetostriction coefficients were determined by parabolically fitting the measured butterfly curves to implement the magnetomechanical calculation. The simulated normalised MFL signals agreed with the experimental ones when the temperature cooled down 30 $^{\circ}C$ from room temperature (20 $^{\circ}C$). It caused an increase of 6.87% in the peak-to-peak amplitude of MFL signal, which was much larger than that in the exclusive temperature condition (2.04%). The temperature cooling down from 60 $^{\circ}C$ to -40 $^{\circ}C$ altered the peak-to-peak values of MFL signals by 35.99%, which could significantly influence the results of defect dimension estimation when the inverse MFL method is employed. To size the defect accurately, the effect of temperature on the MFL signal should be considered in the calibration process. The improved magnetic dipole models could provide valuable tools to understand and evaluate the contribution of temperature and thermal stress on the induced MFL signals. Furthermore, it could be applicable for solving the inverse problem for defect sizing under multiphysics field.

Author statement

Yujue Wang: Conceptualization, Methodology, Writing- Original draft preparation. Yevgen Melikhov: Supervision, Validation, Writing-Reviewing and Editing. Turgut Meydan: Supervision, Investigation, Writing- Reviewing and Editing.

Declaration of competing interest

The authors declare that they have no known competing financial interests or personal relationships that could have appeared to influence the work reported in this paper.

Acknowledgements

This work was supported by Cardiff University and China Scholarship Council (CSC). For the purpose of open access, the authors have applied a Creative Commons Attribution (CC BY) licence (where permitted by UKRI 'Open Government Licence' or 'Creative Commons Attribution No-derivatives (CC BY-ND) licence' may be stated instead) to any Author Accepted Manuscript version arising. Finally, the authors would like to commemorate Dr. Turgut Meydan with this article.

References

[1] Wu B, Wang YJ, Liu XC, He CF. A novel TMR-based MFL sensor for steel wire rope inspection using the orthogonal test method. Smart Mater Struct 2015;24(7).
[2] Liu XC, Wang YJ, Wu B, Gao Z, He CF. Design of tunnel magnetoresistive-based circular MFL sensor array for the detection of flaws in steel wire rope. 2016 J Sens 2016.
[3] Wang ZD, Yao K, Deng B, Ding KQ. Theoretical studies of metal magnetic memory technique on magnetic flux leakage signals. NDT&E Int. 2010;43(4):354–9.
[4] Wang P, Xiong L, Sun Y, Wang H, Tian G. Features extraction of sensor array based PMFL technology for detection of rail cracks. Meas. J. Int. Meas. Confed. 2014;47(1):613–26.
[5] Mandal K, Dufour D, Krause TW, Atherton DL. Investigations of magnetic flux leakage and magnetic Barkhausen noise signals from pipeline steel. J Phys D Appl Phys 1997;30(6):962.
[6] Wang YJ, Liu XC, Wu B, Xiao JW, Wu DH, He CF. Dipole modeling of stress-dependent magnetic flux leakage. NDT&E Int. 2018;95:1–8.
[7] Wang YJ, Meydan T, Melikhov Y, Yang ZC, Wu DH, Wu B, He CF, Liu XC. Stress-dependent magnetic flux leakage: finite element modelling simulations versus experiments. J Nondestr Eval 2020;39(1):1.
[8] Li Y, Tian GY, Ward S. Numerical simulation on magnetic flux leakage evaluation at high speed. NDT&E Int. 2006;39(5):367–73.
[9] Zhang L, Belblidia F, Cameron I, Sienz J, Boat M, Pearson N. Influence of specimen velocity on the leakage signal in magnetic flux leakage type nondestructive testing. J Nondestr Eval 2015;34(2):6.
[10] Raghunathan A, Melikhov Y, Snyder JE, Jiles DC. Theoretical model of temperature dependence of hysteresis based on mean field theory. IEEE Trans Magn 2010;46(6):1507–10.
[11] Raghunathan A, Melikhov Y, Snyder JE, Jiles DC. Modeling the temperature dependence of hysteresis based on Jiles–Atherton theory. IEEE Trans Magn 2009;45(10):3954–7.
[12] Zhang H, Liu Y, Liu S, Lin F. Application of Jiles-Atherton model in description of temperature characteristics of magnetic core. Rev Sci Instrum 2018;89(10):104702.
[13] Li C, Tang Z, Lin G, Lin S, Huang Q. Modeling the temperature dependence of minor hysteresis loops in ferromagnetic materials. Proc. 2016 IEEE Int. Conf. Electron. Inf. Commun. Technol. 2017:505–8.
[14] Dutta SM, Ghorbel FH, Stanley RK. Dipole modeling of magnetic flux leakage. IEEE Trans Magn 2009;45(4):1959–65.
[15] Ding S, Wang P, Lin Y, Zhu D. Reduction of thermal effect on rail stress measurement based on magnetic Barkhausen noise anisotropy. Measurement 2018;125:92–8.
[16] Damljanović V, Weaver RL. Laser vibrometry technique for measurement of contained stress in railroad rail. J Sound Vib 2005;282(1–2):341–66.
[17] Wang YJ, Meydan T, Melikhov Y. Quantitative evaluation of the effect of temperature on magnetic barkhausen noise. Sensors 2021;21(3):898.
[18] Osborn JA. Demagnetising factors of the general ellipsoid. Phys. Rev. 1945;67(11–12):351.
[19] Nowacki W. Thermoelasticity. Elsevier; 2013.
[20] Timoshenko S, Goodier J. Theory of elasticity. the third ed. The McGraw Hill Education; 1970.
[21] Jiles DC. Theory of the magnetomechanical effect. J Phys D Appl Phys 1995;28(8):1537.
[22] Jiles DC. Coupled magnetoelastic theory of magnetic and magnetostrictive hysteresis. IEEE Trans Magn 1993;29(4):2113–23.
[23] Sun Y, Kang Y. A new MFL principle and method based on near-zero background magnetic field. NDT&E Int. 2010;43(4):348–53.
[24] Trevino DA, Dutta SM, Ghorbel FH, Karkoub M. An improved dipole model of 3-D magnetic flux leakage. IEEE Trans Magn 2015;52(12):1–7.
[25] Mierczak L, Jiles DC, Fantoni G. A new method for evaluation of mechanical stress using the reciprocal amplitude of magnetic Barkhausen noise. IEEE Trans Magn 2010;47(2):459–65.
[26] Yamasaki T, Yamamoto S, Hirao M. Effect of applied stresses on magnetostriction of low carbon steel. NDT&E Int. 1996;29(5):263–8.
[27] Jiles DC. Introduction to magnetism and magnetic materials. CRC press; 2015.
[28] Jiles DC, Devine MK. The law of approach as a means of modelling the magnetomechanical effect. J Magn Magn Mater 1995;140–144:1881–2. PART 3.

[29] Grain-Oriented Electrical Steel. Available online: https://www.spacematdb.com/spacemat/manudatasheets/crgo.pdf (accessed on 25 November 2020).
[30] Ultra-Low Expansion Glass-Ceramics. Available online: https://www.sydor.com/wp-content/uploads/2019/05/Ohara-CLEARCERAM-Z-Low-Expansion-Glass.pdf (accessed on 1 November 2020).
[31] Somkun S, Moses AJ, Anderson PI. Effect of magnetostriction anisotropy in non-oriented electrical steels on deformation of induction motor stator cores. IEEE Trans Magn 2009;45(10):4744–7.